



## 3D graphene/AgBr/Ag cascade aerogel for efficient photocatalytic disinfection

Xin Xin<sup>a,b</sup>, Shao-Hai Li<sup>a,b</sup>, Nan Zhang<sup>a,b</sup>, Zi-Rong Tang<sup>b</sup>, Yi-Jun Xu<sup>a,b,\*</sup>

<sup>a</sup> State Key Laboratory of Photocatalysis on Energy and Environment, College of Chemistry, Fuzhou University, Fuzhou, 350116, PR China

<sup>b</sup> College of Chemistry, New Campus, Fuzhou University, Fuzhou, 350116, PR China



### ARTICLE INFO

#### Keywords:

Aerogel  
Reduced graphene oxide  
Silver bromide  
Ag nanoparticles  
Charge transfer

### ABSTRACT

To design semiconductor-based photocatalysts with efficient charge carriers separation and transfer remains an enduring goal of artificial photosynthesis toward target redox reactions. Herein, we report a cascade monolith composite of ternary reduced graphene oxide aerogel/silver bromide/silver (RGA/AgBr/Ag) with efficient charge carriers separation, which exhibits much higher activity than bare AgBr toward photocatalytic bacteria inactivation. Mechanistic studies reveal that the reduced graphene oxide aerogel (RGA) scaffold and Ag nanoparticles serve as electron relay mediators to promote the charge carriers separation and transfer. In addition, the metallic Ag nanoparticles derived from the photoreduction of AgBr during the photocatalytic disinfection can further boost the separation of charge carriers. Control experiments demonstrate that the surface plasmon resonance (SPR)-excited hot electrons of Ag nanoparticles also contribute to enhancing the photoactivity of RGA/AgBr/Ag. As such, the synergy of multiple electron transfer behavior integratively leads to the boosted photocatalytic performance of such RGA/AgBr/Ag aerogel for bacteria inactivation with convenient recyclable operability.

### 1. Introduction

Harvesting solar energy to drive the semiconductor photocatalysis for the elimination of environmental pollution is an ideal strategy to solve the growing worldwide environment crisis in a sustainable way [1–6]. In this regard, silver bromide (AgBr) as a photosensitive semiconductor has been extensively studied due to its superior photocatalytic performance and appropriate band gap corresponding to the visible-light absorption [7–14]. To fully exploit the photoactivity of AgBr for different redox applications, a key factor should be considered—the separation and transfer of photoexcited electrons and holes in AgBr that modulate the efficiency of entire photocatalytic system [15,16]. For this purpose, the loading of cocatalyst, e.g., electrically conductive reduced graphene oxide (RGO), has been commonly employed and the RGO/AgBr powder composites have exhibited enhanced photocatalytic activities compared to bare AgBr [14,17–20]. However, these composite photocatalysts in a powder state have the intrinsic drawback of recyclable operation difficulty from a perspective of practical applications.

Recently, three-dimensional reduced graphene oxide aerogel (3D RGA) has been attracting much attention, since it not only possesses the

intrinsic properties of two-dimensional (2D) RGO sheets, but also provides advanced functions with improved performance in photocatalytic applications [21–24]. Specifically, the 3D network structure of RGA can provide multidimensional electrons transport pathways, which can endow it with high carrier mobility to facilitate the photoexcited electrons transfer [22,25]. Meanwhile, the hierarchical frameworks of RGA make it an ideal scaffold to inhibit the aggregation of subunits, thus exposing more active sites for photocatalytic reaction [26,27]. Furthermore, the macroscopic bulk appearance allows the RGA to be easily separated from a liquid reaction medium, which makes it conveniently recyclable photocatalyst candidate [21,22,26,28].

Herein, we report a facile, low-temperature chemical reduction approach to synthesize ternary aerogel composite by integration of AgBr nanoparticles (NPs) with RGA and plasmonic Ag NPs, which is denoted as reduced graphene oxide aerogel/silver bromide/silver (RGA/AgBr/Ag). In our approach, the 3D RGA plays dual roles in synthesis—possessing hierarchically porous structure to substantially inhibit the aggregation of AgBr NPs and acting as moderate reductant to generate Ag NPs [1,29]. With AgBr as a visible light absorber, the RGA and Ag NPs provide “electron sink” platforms for accepting and transporting electrons, and the improved multichannel electron transfer over

\* Corresponding author at: State Key Laboratory of Photocatalysis on Energy and Environment, College of Chemistry, Fuzhou University, Fuzhou, 350116, PR China.

E-mail address: [yjxu@fzu.edu.cn](mailto:yjxu@fzu.edu.cn) (Y.-J. Xu).

such RGA/AgBr/Ag composite results in higher photocatalytic performance than bare AgBr toward bacteria inactivation. Furthermore, control experiments demonstrate that surface plasmon resonance (SPR)-excited hot electrons of Ag NPs also contribute to enhancing the photoactivity of RGA/AgBr/Ag composite. Accordingly, the mechanism of the ternary RGA/AgBr/Ag composite for photocatalytic disinfection is proposed.

## 2. Experimental section

### 2.1. Materials

Cetyltrimethyl ammonium bromide (CTAB) was supplied by Sigma-Aldrich. Sodium Hydrogen Sulfite ( $\text{NaHSO}_3$ ) was obtained from J&K Scientific. Silver nitrate ( $\text{AgNO}_3$ ), absolute ethanol ( $\text{C}_2\text{H}_5\text{OH}$ ), hydrochloric acid (HCl), concentrated sulfuric acid ( $\text{H}_2\text{SO}_4$ , 98%), potassium permanganate ( $\text{KMnO}_4$ ), hydrogen peroxide ( $\text{H}_2\text{O}_2$ , 30%) and N, N-dimethylformamide ( $\text{C}_3\text{H}_7\text{NO}$ , DMF) were obtained from Sinopharm Chemical Reagent Co., Ltd. (Shanghai, China). Graphite powder was supplied by Qingdao Zhongtian Company, China. All materials were used as received without further purification. Deionized (DI) water used in the synthesis process was obtained from local sources.

### 2.2. Synthesis

#### 2.2.1. Preparation of graphene oxide (GO)

GO was prepared from natural graphite powder by a modified Hummers method [30,31]. The details were presented in the Supporting Information.

#### 2.2.2. Preparation of reduced graphene oxide hydrogel (RGH)

The RGH was synthesized by a facile chemical reduction method [32]. Typically, 15 mL of GO (2 mg  $\text{mL}^{-1}$ ) and 2 mL of  $\text{NaHSO}_3$  (60 mg  $\text{mL}^{-1}$ ) solution were mixed in a dried beaker with a capacity of 50 mL, and then kept at 70 °C for 12 h. After being cooled to room temperature, the RGH was dialyzed with DI water for 24 h.

#### 2.2.3. Preparation of reduced graphene oxide aerogel/silver bromide/silver composite (RGA/AgBr/Ag)

The RGA/AgBr/Ag was synthesized according to the previous reports with minor modifications [33,34]. The obtained RGH was immersed into 10 mL solution of CTAB (8 mL DI water and 2 mL ethanol) at 60 °C for 6 h. After being cooled to room temperature, the RGH/CTAB was washed with ethanol and DI water for several times. Afterwards, 38 mg  $\text{AgNO}_3$  was dissolved in 10 mL DI water and the RGH/CTAB was immersed into  $\text{AgNO}_3$  solution for 12 h. The finally synthesized RGH/AgBr/Ag was washed by DI water for several times and treated by freeze-drying, and then the RGA/AgBr/Ag composite was obtained. Since the bare RGA was firstly produced during the synthetic process of RGA/AgBr/Ag, the final content of AgBr and Ag can be estimated through the quantity of RGA/AgBr/Ag minus bare RGA (Fig. S1). For the control experiments, bare AgBr and binary RGA/Ag were prepared through the same procedures without the addition of RGH and CTAB, respectively.

### 2.3. Characterizations

The morphology of the samples was determined by field emission scanning electron microscopy (FE-SEM) on a FEI Nova NANOSEM 230 spectrophotometer. Transmission electron microscopy (TEM) images were collected using a JEOL Model JEM 2010 EX microscope at an accelerating voltage of 200 kV. The X-ray diffraction (XRD) patterns of the samples were collected on a Bruker D8 Advance X-ray diffractometer with Ni-filtered Cu K $\alpha$  radiation at 40 kV and 40 mA in the 2  $\theta$  ranging from 10° to 80° with a scan rate of 0.02° per second. X-ray photoelectron spectroscopy (XPS) analysis was completed on a Thermo

Scientific ESCA Lab 250 spectrometer equipped with a mono chromatic Al K $\alpha$  (X-ray source), a multiaxial sample stage and a hemispherical analyzer. The binding energies obtained in the XPS analysis were calibrated for specimen charging by referencing C 1 s to 284.6 eV. The photoluminescence spectra (PL) for samples were analyzed on an Edinburgh Analytical Instrument F980 spectrophotometer with an excitation wavelength of 250 nm. To ensure the comparability of the PL spectra, the experimental parameters, including the excitation wavelength, slit width, and the amount of the samples, were identical. The concentration of silver ions in treated cell suspension was examined by inductively coupled plasma optical emission spectrometer (ICP-OES, OPTIMA 8000).

The electrochemical analysis was conducted in a conventional three electrode cell, which used a Pt plate as the counter electrode and an Ag/AgCl electrode as the reference electrode. The working electrode was prepared on fluorine doped tin oxide (FTO) glass that was cleaned by sonication in ethanol and dried at 80 °C for 2 h. The boundary of FTO glass was protected using Scotch tape. The 3 mg sample was fully dispersed in 0.5 mL of DMF by sonication to get slurry. The slurry was spread onto the pre-treated FTO glass. After air drying, the working electrode was further dried at 120 °C for 2 h to improve adhesion. The exposed area of the working electrode was 0.28 cm<sup>2</sup>. The electrochemical impedance spectroscopy (EIS) measurement was measured via an EIS spectrometer (CHI-660D workstation, CH Instrument) in the three-electrode cell in the presence of 0.5 M KCl solution containing 5.0 mM  $\text{K}_3[\text{Fe}(\text{CN})_6]$ /K<sub>4</sub>Fe(CN)<sub>6</sub> by applying an AC voltage with 5 mV amplitude in a frequency range from 1 Hz to 100 kHz under open circuit potential conditions. The cyclic voltammograms were measured in the same solution in the three electrode cell as that of the EIS measurement on the BAS Epsilon workstation. The cathodic polarization curves were obtained using the linear sweep voltammetry technique with a scan rate of 0.2 mV s<sup>-1</sup>.

The bacteria death analysis was ascertained by fluorescent-based cell live/dead test. The treated bacteria were collected at different time intervals (0, 10 and 20 min) and subsequently stained with a mixture of propidium iodide (PI, Sigma-Aldrich, 1  $\mu\text{g mL}^{-1}$ ) and 4,6-diamidino-2-phenylindole (DAPI, Sigma-Aldrich, 5  $\mu\text{g mL}^{-1}$ ) for 10 min. Then they were centrifuged (8000 rpm, 5 min) and washed three times with sterile phosphate-buffered saline (PBS) solution. The samples were imaged using a Nikon A1 confocal microscope with a 60x objective. The changes of structure and morphology of bacteria were determined by SEM (JEOL-JSM-6380LV). Typically, the treated bacteria at different irradiation time intervals (0, 10 and 20 min) were transferred onto poly-lysine coated cover-slips and subsequently fixed with 2% osmium tetroxide. The samples were sequentially dehydrated with 30, 50, 70, 90, and 100% ethanol for 30 min, respectively. Then the obtained samples were lyophilized, gold sputter-coated before SEM analysis.

### 2.4. Photoactivity

The photoactivity of the samples was evaluated by the inactivation of *Escherichia coli* (*E. coli*) under visible light irradiation. Prior to the experiments, all glass apparatuses used in the experiments were autoclaved at 121 °C for 30 min to ensure sterility. In a typical reaction, 4 mL bacterial stock solution was added into 36 mL PBS buffer (pH = 7.4), and the samples were added into the above cell suspension after complete mixture. The initial viable cell concentration was about  $10^6$ – $10^7$  colony forming units (CFU)  $\text{mL}^{-1}$ . The cell suspension was gently stirred throughout the entire photocatalytic procedure. A 300 W Xe arc lamp (PLS-SXE 300C, Beijing Perfect light Co., Ltd.), emitting visible light ( $\lambda > 400$  nm) with an energy output of 0.383 W  $\text{cm}^{-2}$  measured by a Thorlabs PM100 optical power and energy meter, was placed at a distance of approximate 5 cm from the reactor to be the irradiation source. The temperature of the reactor was maintained at 25 °C by a flow of cooling water during the photocatalytic reaction. At certain irradiation time interval during the experiment, 0.5 mL solution

was drawn from the system and then serially diluted with PBS buffer to yield the viable cell density. After dilution to a suitable concentration with PBS buffer, the cell suspension was quickly spread on Luria-Bertani broth agar culture plates and cultured at 37 °C for 24 h. The survival rate was estimated by the plate count method. Control experiments with addition of radical scavengers were carried out similar to the above photocatalytic inactivation of *E. coli* except the control reaction conditions.

### 2.5. Recycling tests of the RGA/AgBr/Ag composite

The recycling tests of the synthesized aerogel catalyst were done as follows. Typically, when a photocatalytic cycle was finished, the used RGA/AgBr/Ag was washed repeatedly with DI water and then immersed into DI water at room temperature for 12 h. Finally, the RGA/AgBr/Ag was washed thoroughly with sterile PBS solution prior to the next cycle. Between the two cycles, it was unnecessary to perform tedious centrifugation, sonication, and drying processes [35].

## 3. Results and discussion

The fabrication of RGA/AgBr/Ag is schematically illustrated in Fig. 1A. Firstly, the reduced graphene oxide hydrogel (RGH) has been synthesized through the low-temperature chemical reduction approach with NaHSO<sub>3</sub> as the reductant [32] and then modified with the cetyltrimethyl ammonium bromide (CTAB) for the loading of AgBr [33,34]. The introduction of NaHSO<sub>3</sub> can cause partial removal of oxygen-containing hydrophilic groups of GO and an increase of the hydrophobicity and the π-conjugated structures of RGO. The hydrophilic-hydrophobic balance enables assembly of RGO to form an integrated hydrogel

[24,32,36]. Subsequently, the simultaneous achievement of reduction of Ag<sup>+</sup> ions and loading of AgBr in silver nitrate (AgNO<sub>3</sub>) solution leads to the uniform distribution of Ag and AgBr NPs within the 3D scaffold of RGH support [33,34,37]. Finally, the reduced graphene oxide hydrogel/silver bromide/silver (RGH/AgBr/Ag) is dehydrated by the freeze-drying process to form the RGA/AgBr/Ag aerogel composite.

The morphology of samples has been characterized by scanning electron microscopy (SEM). As seen from Fig. S2A, the bare RGA shows an interconnected porous framework with random open pores constructed from the cross-linking of the RGO sheets. With regard to RGA/AgBr/Ag composite, it can be observed from Fig. 1B and C that the AgBr NPs are evenly distributed throughout the RGO sheets surface of the RGA. The Ag NPs are hardly observed in the SEM images of RGA/AgBr/Ag due to their relatively low contents and small size. The magnified SEM image (Fig. 1C) of RGA/AgBr/Ag indicates that the average particle size of AgBr NPs is ca. 80 nm, and the size distribution histogram is plotted in the inset of Fig. 1C. For comparison, AgBr without RGA is also synthesized and the corresponding SEM images are shown in Fig. S2B and C. It is clear to see that the bare AgBr NPs obtained in the absence of RGA display irregular shaped blocks with the size range of 0.3–1.1 μm (Fig. S2D), which is much larger than the AgBr NPs in RGA/AgBr/Ag composite. Therefore, the introduction of the RGA substantially inhibits the aggregation of AgBr during the synthesis process.

To further glean the microscopic structure of the samples, the transmission electron microscopy (TEM) analysis of RGA/AgBr/Ag has been performed. Fig. 1D shows the TEM image of RGA/AgBr/Ag composite, from which it can be seen that the AgBr and Ag NPs are individually assembled onto the RGO sheets surface of RGA. The high-resolution TEM (HRTEM) analysis of RGA/AgBr/Ag shows the identified lattice spacing of 0.28 nm, corresponding to the (200) crystal plane

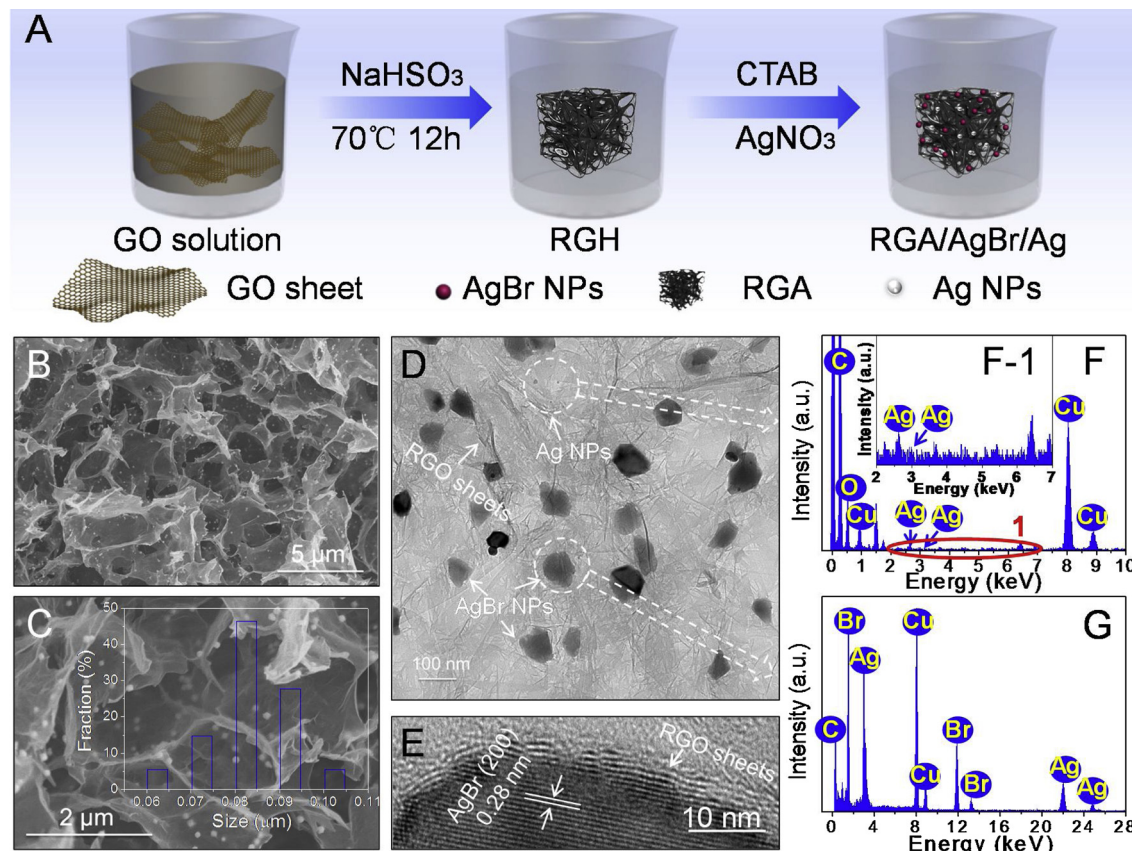
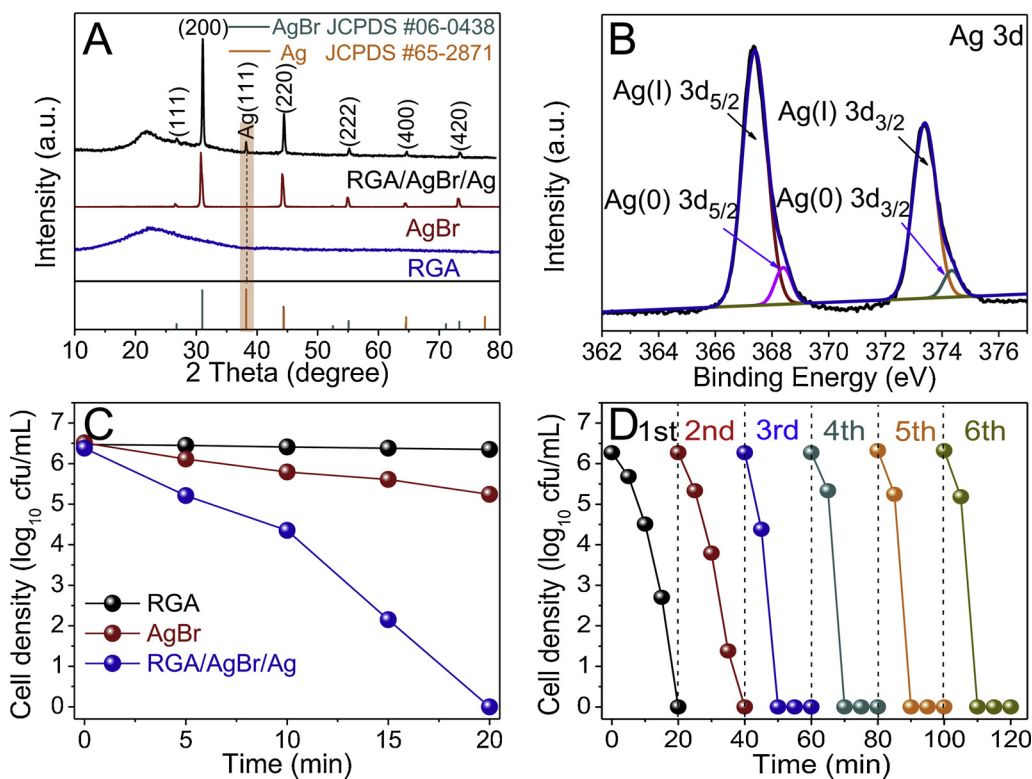


**Fig. 1.** (A) Flowchart for the fabrication of RGA/AgBr/Ag aerogel composite. (B, C) SEM images of RGA/AgBr/Ag, the inset of (C) is particle size distribution histogram of AgBr NPs. (D) TEM and (E) HRTEM images of RGA/AgBr/Ag and AgBr. (F, G) The EDX spectroscopy of RGA/AgBr/Ag. For better clarity, the local regions of the EDX spectra indicated by the red oval in (F) is enlarged as (F-1), the inset of (F) is the enlarged EDX spectra. (For interpretation of the references to colour in this figure legend, the reader is referred to the web version of this article).



of AgBr (Fig. 1E) [17]. The RGO sheets can also be clearly seen in the edge area of the AgBr (Fig. 1E). The energy-dispersive X-ray (EDX) results (Fig. 1F and G) of selected areas from Fig. 1D further corroborate the presence of Ag and AgBr NPs on the RGA scaffold. For clarity, the partially enlarged EDX results from Fig. 1F are presented as Fig. 1F-1, from which the signals of element Ag are clearly identified. In addition, as revealed by the elemental mapping results of RGA/AgBr/Ag composite in Fig. S3, the elements Ag and Br are evenly distributed on the RGA. The above results illustrate the successful incorporation of RGA and Ag NPs into the AgBr matrix, thereby forming the ternary RGA/AgBr/Ag aerogel composite.

X-ray diffraction (XRD) and X-ray photoelectron spectroscopy (XPS) measurements have been employed to further analyze the structure and element composition of samples. Fig. 2A depicts the XRD patterns of RGA, AgBr and RGA/AgBr/Ag. The main diffraction peaks at 2  $\theta$  values of 26.7°, 30.9°, 44.4°, 55.0°, 64.5°, and 73.3° can be respectively indexed to (111), (200), (220), (222), (400), and (420) crystal planes of AgBr phase (JCPDS No. 06-0438). The wide diffraction peak around at 22.5° is observed in the RGA and RGA/AgBr/Ag composite, which corresponds to the RGO characteristic diffraction peak and indicates the effective reduction of GO [22,26,38,39]. It should be noted that one additional peak located at 38.1° is observed in RGA/AgBr/Ag, which can be indexed to the (111) crystal plane of metallic Ag (JCPDS No. 65-2871). The presence of metallic Ag can be further evidenced by XPS measurement. As mirrored in Fig. 2B, the two doublet 3d peaks in the high-resolution spectrum of Ag 3d suggest that there are two different elemental chemical states of Ag species. The Ag 3d<sub>5/2</sub> and Ag 3d<sub>3/2</sub> peaks with binding energies of 367.3 and 373.4 eV are ascribed to the Ag(I) in AgBr, and the other doublet at 368.4 and 374.3 eV for Ag 3d<sub>5/2</sub> and Ag 3d<sub>3/2</sub> are assigned to the metallic Ag [14,40,41]. The XPS results along with the above XRD and TEM results clearly indicate that the Ag NPs are well assembled on RGA scaffold. The full spectrum of RGA/AgBr/Ag in Fig. S4 reveals the existence of C, Ag, O and Br elements in the RGA/AgBr/Ag composite, which is in agreement with the EDX results as discussed above.

We then set out to investigate the photocatalytic performance of

**Fig. 2.** (A) XRD patterns of RGA, AgBr and RGA/AgBr/Ag. (B) XPS spectra of Ag 3d. (C) Photocatalytic disinfection efficiencies toward *E. coli* ( $10^{6.37}$  colony forming units (CFU) mL<sup>-1</sup>) with the RGA, AgBr and RGA/AgBr/Ag under visible light ( $\lambda > 400$  nm) irradiation. (D) Recycling experiments of RGA/AgBr/Ag for photocatalytic inactivation of *E. coli* cells ( $10^{6.37}$  CFU mL<sup>-1</sup>).

samples by the inactivation of *Escherichia coli* (*E. coli*, a Gram-negative bacterium) cells under visible light irradiation ( $\lambda > 400$  nm). Control experiments in the absence of either photocatalyst or light irradiation show no disinfection efficiencies, indicating that the photocatalyst itself and visible-light irradiation have almost no cytotoxicity to *E. coli* cells (Fig. S5). Fig. 2C shows the photoactivity of RGA, AgBr and RGA/AgBr/Ag for the inactivation of *E. coli* cells under identical reaction conditions. We can see that bare AgBr exhibits antimicrobial activity with  $10^{1.41}$  colony forming units (CFU) mL<sup>-1</sup> decrease of viable cell density within 20 min. The bare RGA does not show antimicrobial activity against *E. coli* cells upon visible light irradiation for 20 min, indicating its negligible bactericidal role. Notably, the simultaneous introduction of RGA and Ag NPs into the AgBr matrix leads to an obvious photoactivity improvement, which can complete inactivation of  $1.0 \times 10^{6.37}$  CFU mL<sup>-1</sup> of *E. coli* cells under visible light irradiation for 20 min (Fig. 2C and S6).

Additionally, the recycling experiments results reveal that the photoactivity of the RGA/AgBr/Ag has a distinct growth trend along with the increase of the cycling number in the first four recycle times (Fig. 2D). This should be attributed to the contribution of the “electron sink” effect of Ag NPs originated from the photoreduction of AgBr during the photocatalytic reaction, as observed in AgBr-based photocatalytic systems [19,33,42,43]. Simultaneously, owing to the presence of RGA and Ag NPs as electrons mediators, the surface electrons of AgBr are apt to inject into RGA and Ag NPs instead of continuously reduce Ag<sup>+</sup> ions to metallic Ag, and thus, the photoactivity of RGA/AgBr/Ag keeps nearly unchanged in the last two recycle times (Fig. 2D) [7,11,14,33,42,44]. It can thus be reasonably inferred that the content of metallic Ag reaches a maximum after four cycles, as the photocatalytic activity reaches a maximum [33,42]. XRD and XPS results also support the increased contents of metallic Ag in RGA/AgBr/Ag composite after the photocatalytic reaction (Fig. S7A and B). It is worth noting that during the whole recycling process, the RGA/AgBr/Ag can be easily separated and recycled from the aqueous reaction medium with a tweezer (Fig. S8). In addition, in view of the fact that there may be Ag<sup>+</sup> ions leaked during the photocatalytic process because of the

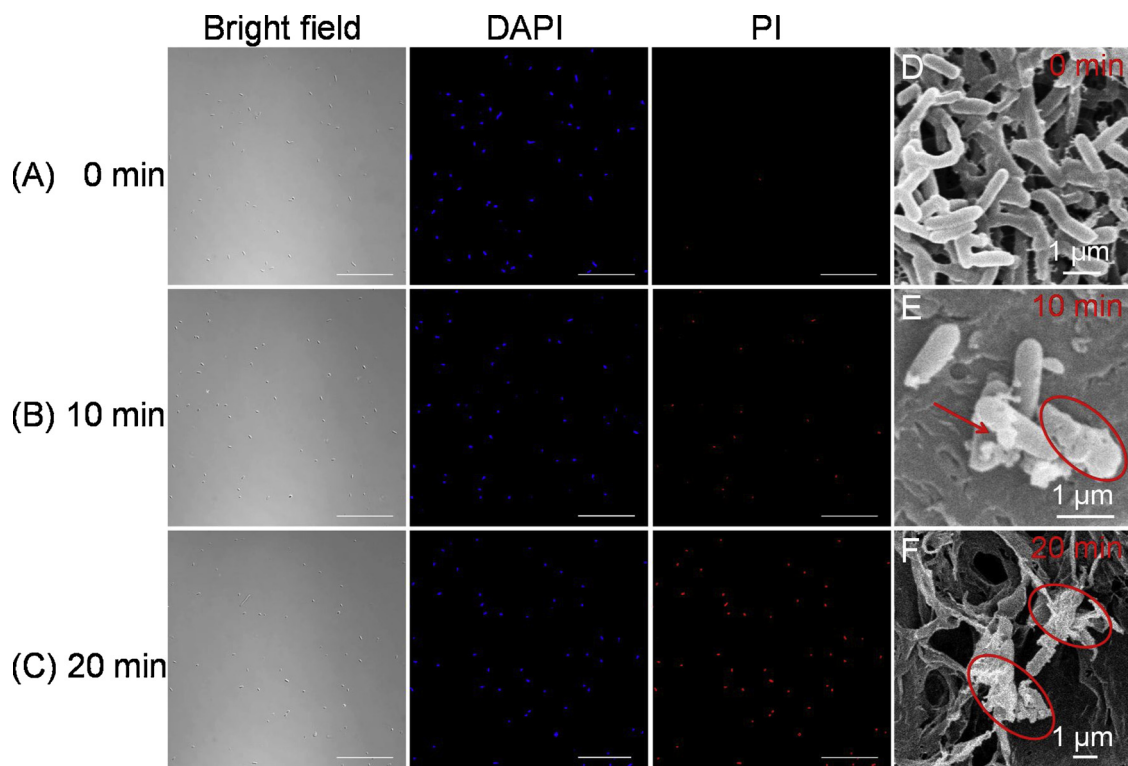


**Fig. 3.** (A–C) Confocal fluorescent images of live and dead *E. coli* cells ( $10^{6.37}$  CFU mL $^{-1}$ ), the scale bar is 50  $\mu$ m. SEM images of *E. coli* cells treated with RGA/AgBr/Ag under visible light: (D) 0 min, (E) 10 min, (F) 20 min.

high oxidative power of the formed reactive species [45], we further investigate the concentration of Ag $^{+}$  ions in treated cell suspension and their antimicrobial activity. The results show that the very low concentration of Ag $^{+}$  ions is 0.77 mg L $^{-1}$  after 20 min of visible light irradiation, which exhibits low antimicrobial activity with only  $10^{0.28}$  CFU mL $^{-1}$  cells' loss under the same experimental condition (Fig. S9). Along with experimental result from the dark reaction test on RGA/AgBr/Ag, it is reasonable to infer that the intrinsic disinfection properties of Ag (Ag NPs and Ag $^{+}$  ions) [46] can only cause very limited bacterial inactivation in this photocatalytic system. These also suggest that the slight leaking of Ag $^{+}$  ions does not have a significant effect on the stable recycling photoactivity of RGA/AgBr/Ag.

The photocatalytic disinfection effect of RGA/AgBr/Ag toward *E. coli* cells has been further confirmed by laser scanning fluorescence microscopy [45–47]. The propidium iodide (PI) and 4,6-diamidino-2-phenylindole (DAPI) have been employed to stain *E. coli* cells. DAPI is a blue-fluorescent stain labeling both live and dead cells, whereas PI is a red-fluorescent stain labeling only dead cells with compromised or damaged cell membranes [45–47]. As shown in Fig. 3A, there are almost no cells stained by PI at 0 min. When treated with RGA/AgBr/Ag under visible-light irradiation for 10 min, some of the cells display red fluorescence (Fig. 3B), indicating that the integrities of these cells have been destroyed [13,45]. After 20 min, the PI-stained red fluorescent bacteria increase greatly (Fig. 3C), indicating that a large proportion of bacteria are killed by the RGA/AgBr/Ag [46]. Additionally, the changes of structure and morphology of *E. coli* cells at different time intervals of this disinfection process have been visually observed by SEM [45–47]. The original *E. coli* cells are representatively rod-shaped with smooth and intact cell membrane, as shown in Fig. 3D [45,47]. After treatment with RGA/AgBr/Ag under visible light for 10 min, the adsorbed bacteria gradually become deformed, and some of the bacteria appear to have obvious cell rupture and aggregation (Fig. 3E), indicating that the active species generated by RGA/AgBr/Ag aerogel participate in photocatalytic disinfection progress of *E. coli* cells [47]. In Fig. 3F, it is hard to distinguish their original morphology after 20 min of visible light

irradiation, indicating the *E. coli* cells embedded in the RGA/AgBr/Ag aerogel are effectively inactivated.

The photocatalytic performance of semiconductor materials is closely related to the charge carriers separation and transfer process [15,48,49]. In order to disclose the underlying reason for the enhanced photoactivity of RGA/AgBr/Ag composite toward bacteria inactivation as compared with the bare AgBr, a series of joint photoelectrochemical and photoluminescence characterizations have been carried out for in-depth exploitations. As displayed in Fig. 4A, the cyclic voltammograms (CV) of AgBr and RGA/AgBr/Ag electrodes show two reversible anodic and cathodic peaks corresponding to the one-electron redox process [31]. Considering that the preparation of the electrodes and electrolyte are identical for the measurements, the current density of the electrodes is related to the electron transfer rate of the electrode materials [15,26,49,50]. It can therefore be found that the introduction of RGA and Ag NPs into AgBr matrix can boost the electrons transfer across the contact interface between electrode and electrolyte solution. The polarization curves in Fig. 4B indicate the same tendency of charge transfer enhancement. To further determine the advantage of RGA/AgBr/Ag over AgBr in improving the charge carriers transfer, electrochemical impedance spectra (EIS), as a useful tool to characterize the charge carriers migration of the electrode materials [31,38,49,50], has also been measured for AgBr and RGA/AgBr/Ag electrodes, and the results are displayed in Fig. 4C. The RGA/AgBr/Ag possesses more depressed semicircle at high frequency than bare AgBr, manifesting the more efficient transfer of charge carriers is obtained over the RGA/AgBr/Ag than that over bare AgBr [51,52]. The photoluminescence (PL) spectrum conducted under 250 nm monochromatic light excitation has been employed to gain more hints on the fate of charge carriers photoexcited from AgBr. As shown in Fig. 4D, the addition of RGA and Ag NPs into the AgBr matrix can decrease the PL intensity, suggesting the efficient inhibition of radiative recombination of electron-hole pairs in the composite of RGA/AgBr/Ag [31]. The above results together suggest that the coexistence of RGA and Ag NPs is able to synergistically promote the efficient separation and transfer of charge carriers

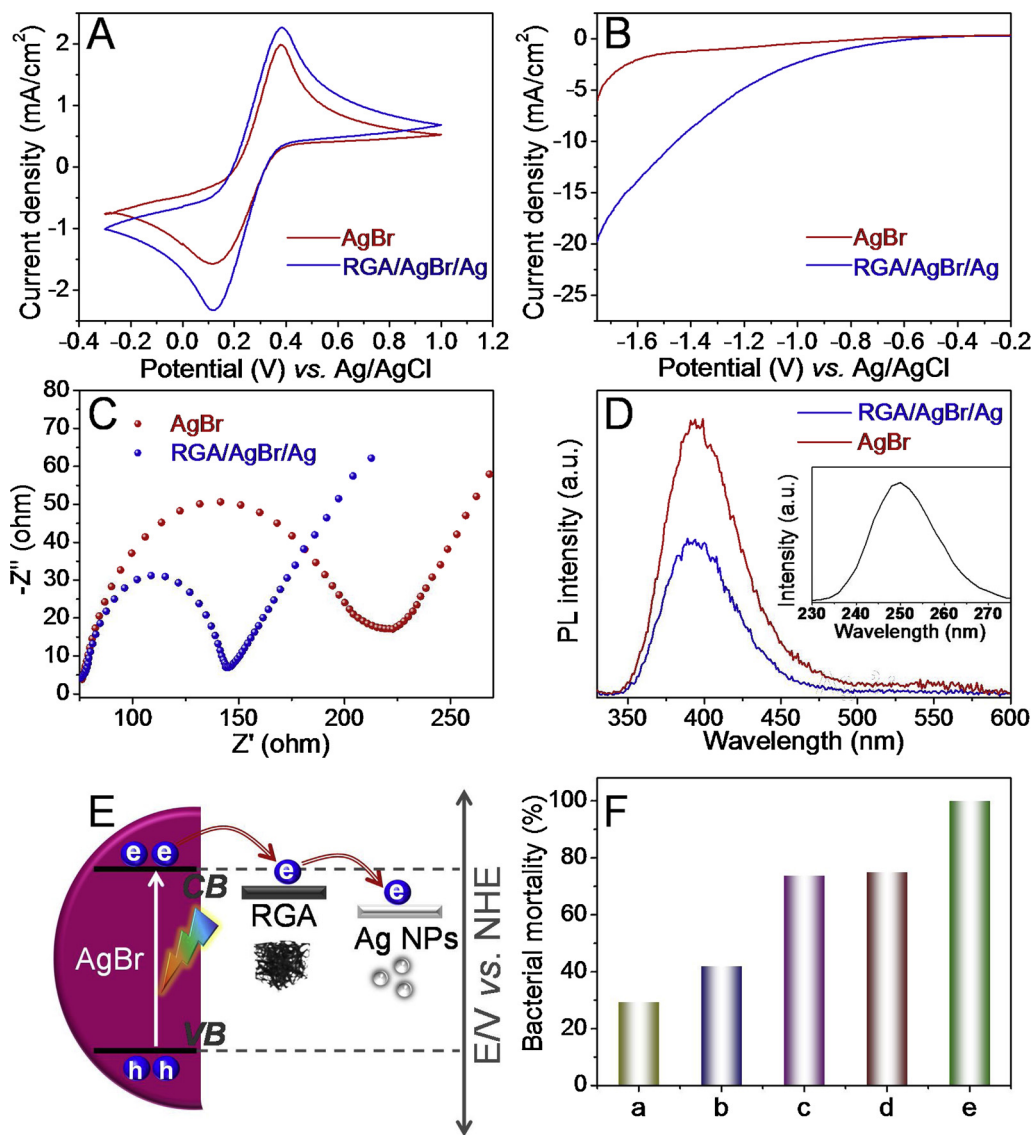


**Fig. 4.** (A–C) Cyclic voltammograms, polarization curves and electrochemical impedance spectroscopy (EIS) Nyquist plots of RGA/AgBr/Ag and AgBr. (D) Photoluminescence (PL) emission spectra with an excitation wavelength of 250 nm, inset of (D) is the PL excitation spectrum of AgBr. (E) Schematic illustration of RGA/AgBr/Ag enhanced charge transfer of AgBr. (F) Control experiments for photocatalytic inactivation of *E. coli* cells ( $10^{6.37}$  CFU mL<sup>-1</sup>) over RGA/AgBr/Ag: (a) reaction with sodium oxalate as a scavenger for holes, (b) reaction with hexavalent chromium Cr(VI) as a scavenger for electrons, (c) reaction with 4-hydroxy-2,2,6,6-tetramethylpiperidinyloxy (TEMPO) as a scavenger for superoxide radical, (d) reaction with isopropanol as a scavenger for hydroxyl radical and (e) reaction without scavenger.

photogenerated from the excitation of AgBr under visible light irradiation, as illustrated in Fig. 4E.

On the other hand, as a typical plasmonic metal, Ag NPs have been widely used as an antenna under visible light illumination to generate hot charge carriers, which subsequently induce the photocatalytic reactions [7,33,41,52–56]. To investigate the possible contribution of the SPR-excited hot electrons of Ag NPs in our composite photocatalyst, further control investigations have been performed. Considering that the absorption peak of AgBr NPs is overlapped with the plasmonic resonance band of Ag NPs [33,55,57]. In such a case, it is difficult to determine the exact generation sites of electrons. Therefore, we use the binary RGA/Ag composite as model catalyst to exclude the influence of AgBr. The preparation method of RGA/Ag is the same as the synthesis of ternary RGA/AgBr/Ag composite except the addition of CTAB. Specifically, the RGA/Ag has been prepared by the facile chemical reduction approach, as evidenced in Fig. S10 and S11. The control experiment with adding hexavalent chromium (Cr(VI)) as a quenching agent for electrons over the RGA/Ag has been performed, as shown in Fig. S12. It has been observed that the disinfection efficiency of RGA/Ag is distinctly suppressed with the addition of Cr(VI) in the reaction system, implying that the plasmonic hot electrons of Ag NPs are able to participate in the photocatalytic disinfection process. Therefore, the SPR-excited hot electrons of Ag NPs contribute to the enhanced

photocatalytic performance of RGA/AgBr/Ag for disinfection under visible light irradiation.

Control experiments using different radical scavengers help us to further understand the reaction mechanism of the inactivation of *E. coli* cells over RGA/AgBr/Ag composite under visible light irradiation ( $\lambda > 400$  nm) (Fig. 4F). Before conducting the experiments, the applied concentrations of each scavenger have been optimized to ensure their best scavenging effect and not cause any inactivation to the normal *E. coli* cells [47,58]. It can be seen from Fig. 4Fa and b, the obvious inhibition effects of bacterial inactivation are observed when sodium oxalate and Cr(VI) are added to quench holes and electrons, respectively, which confirms the pivotal roles of holes and electrons in this photocatalytic disinfection process. On one hand, the photoexcited electrons and holes could directly attack the bacteria themselves [47]. On the other hand, they could possibly be transformed into other reactive species, such as superoxide radical and hydroxyl radical ( $\cdot\text{OH}$ ), to oxidize the outer membrane of *E. coli* bacteria [12,47,59]. The control experimental results with the addition of 4-hydroxy-2,2,6,6-tetramethylpiperidinyloxy (TEMPO) and isopropanol, as superoxide radical and  $\cdot\text{OH}$  scavenger respectively, reveal that they have relatively moderate effect on the photocatalytic disinfection process over RGA/AgBr/Ag (Fig. 4Fc and d). The above results indicate that electrons and holes play the dominant role in photocatalytic inactivation of *E. coli* bacteria,

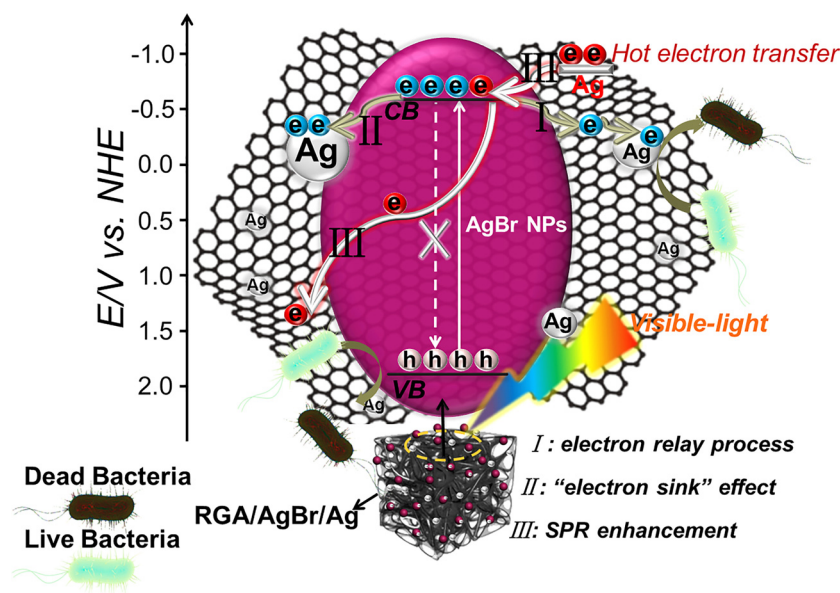


**Fig. 5.** Illustration of the proposed reaction mechanism for the photocatalytic inactivation of *E. coli* cells over RGA/AgBr/Ag under visible light irradiation.

and other reactive oxygen species, including ·OH and superoxide radical, collectively take part in the photocatalytic disinfection process.

Based on the above discussions, a tentative reaction mechanism for the inactivation of *E. coli* cells over cascade RGA/AgBr/Ag aerogel composite can be proposed, as illustrated in Fig. 5. Under the illumination of visible light, AgBr NPs in the RGA/AgBr/Ag composite photocatalyst are photoexcited to generate electron-hole pairs. Due to the introduction of RGA as an electron conductive platform, the electrons can easily transfer to the RGO sheets of RGA from the conduction band (CB) of AgBr. Subsequently, the Ag NPs supporting on the RGO sheets with low Fermi level can further trap the electrons accumulated in RGO sheets. Such an electron relay process efficiently improves the fate and transfer of photogenerated electrons, thereby resulting in the enhanced photoactivity of the RGA/AgBr/Ag composite under visible light irradiation. Simultaneously, the remaining photogenerated holes can directly participate in the inactivation of *E. coli* cells. During the next recycling experiments of RGA/AgBr/Ag, the Ag NPs gradually generate from the photoreduction of AgBr, which acting as “electron sink” could capture and transfer the excited electrons in the CB of AgBr, resulting in further improved photoactivity toward inactivation of *E. coli* cells. In addition, due to the SPR effect of Ag NPs, the generated plasmonic hot electrons of Ag NPs are able to be extracted for participating in the photocatalytic reaction, which also can contribute to improving the photoactivity of the RGA/AgBr/Ag. To further explore the potential application of the RGA/AgBr/Ag ensemble, the activity of the composite toward photocatalytic degradation of methyl orange (MO) dye has been tested. The results in Fig. S13 reveal that the RGA/AgBr/Ag exhibits more efficient photoactivity for MO degradation than bare RGA and AgBr.

#### 4. Conclusion

In summary, we have constructed a ternary aerogel composite consisting of AgBr and Ag NPs decorated on the RGA scaffold via a low-temperature chemical reduction approach. This RGA/AgBr/Ag composite exhibits much higher activity than bare AgBr toward photocatalytic bacteria inactivation. It has been revealed that the formation of electron relay process between AgBr, RGA and Ag NPs exerts a profound influence on the separation of photogenerated charge carriers leading to the enhanced photoactivity of RGA/AgBr/Ag. The “electron sink” effect of the Ag NPs formed from the photoreduction of AgBr during the photocatalytic disinfection results in further enhanced

charge transfer and boosted photoactivity. Furthermore, the SPR-excited hot electrons of Ag NPs are also beneficial for enhancing the photoactivity of RGA/AgBr/Ag. In addition, the RGA/AgBr/Ag composite also displays excellent recyclability and operability during the successive recycling activity tests. The ternary cascade system featuring multichannel-enhanced charge-carrier separation and transfer as well as its monolith aerogel structure is expected to provide a promising avenue for constructing highly efficient AgBr-based photocatalytic systems toward environmental applications.

#### Acknowledgements

The support from the National Natural Science Foundation of China (NSFC) (21872029, U1463204, 21173045), the Award Program for Minjiang Scholar Professorship, the Natural Science Foundation (NSF) of Fujian Province for Distinguished Young Investigator Rolling Grant (2017J07002), the Independent Research Project of State Key Laboratory of Photocatalysis on Energy and Environment (NO. 2014A05), the 1st Program of Fujian Province for Top Creative Young Talents, and the Program for Returned High-Level Overseas Chinese Scholars of Fujian province is gratefully acknowledged.

#### Appendix A. Supplementary data

Supplementary material related to this article can be found, in the online version, at doi:<https://doi.org/10.1016/j.apcatb.2018.12.066>.

#### References

- [1] N. Zhang, M.-Q. Yang, S. Liu, Y. Sun, Y.-J. Xu, Chem. Rev. 115 (2015) 10307–10377.
- [2] X. Li, W. Zhang, J. Li, G. Jiang, Y. Zhou, S. Lee, F. Dong, Appl. Catal. B 241 (2019) 187–195.
- [3] K. Li, P. Chen, J. Li, Y. Sun, Y. Chu, F. Dong, Catal. Sci. Technol. 8 (2018) 4600–4603.
- [4] J. Li, Z. Zhang, W. Cui, H. Wang, W. Cen, G. Johnson, G. Jiang, S. Zhang, F. Dong, ACS Catal. 8 (2018) 8376–8385.
- [5] L. Chen, R. Huang, M. Xiong, Q. Yuan, J. He, J. Jia, M.-Y. Yao, S.-L. Luo, C.-T. Au, S.-F. Yin, Inorg. Chem. 52 (2013) 11118–11125.
- [6] L. Chen, J. He, Q. Yuan, Y. Liu, C.-T. Au, S.-F. Yin, J. Mater. Chem. A 3 (2015) 1096–1102.
- [7] J. Jiang, H. Li, L. Zhang, Chem. Eur. J. 18 (2012) 6360–6369.
- [8] K. Ding, D. Yu, W. Wang, P. Gao, B. Liu, Appl. Surf. Sci. 445 (2018) 39–49.
- [9] X.-J. Wen, C.-G. Niu, H. Guo, L. Zhang, C. Liang, G.-M. Zeng, J. Catal. 358 (2018) 211–223.
- [10] F. Chen, H. Huang, C. Zeng, X. Du, Y. Zhang, ACS Sustain. Chem. Eng. 5 (2017)

- 7777–7791.
- [11] F. Chen, W. An, L. Liu, Y. Liang, W. Cui, *Appl. Catal. B* 217 (2017) 65–80.
  - [12] L.-S. Zhang, K.-H. Wong, H.-Y. Yip, C. Hu, J.C. Yu, C.-Y. Chan, P.-K. Wong, *Environ. Sci. Technol.* 44 (2010) 1392–1398.
  - [13] D. Xia, T. An, G. Li, W. Wang, H. Zhao, P.K. Wong, *Water Res.* 99 (2016) 149–161.
  - [14] M. Zhu, P. Chen, M. Liu, *ACS Nano* 5 (2011) 4529–4536.
  - [15] L. Yuan, B. Weng, J.C. Colmenares, Y. Sun, Y.-J. Xu, *Small* 13 (2017) 1702253.
  - [16] N. Zhang, R. Ciriminna, M. Pagliaro, Y.-J. Xu, *Chem. Soc. Rev.* 43 (2014) 5276–5287.
  - [17] L. Zhang, Y. Shi, L. Wang, C. Hu, *Appl. Catal. B* 220 (2018) 118–125.
  - [18] B. Cai, X. Lv, S. Gan, M. Zhou, W. Ma, T. Wu, F. Li, D. Han, L. Niu, *Nanoscale* 5 (2013) 1910–1916.
  - [19] Y. Yang, W. Zhang, R. Liu, J. Cui, C. Deng, *Sep. Purif. Technol.* 190 (2018) 278–287.
  - [20] M. Zhu, P. Chen, M. Liu, *Langmuir* 28 (2012) 3385–3390.
  - [21] K.-Q. Lu, X. Xin, N. Zhang, Z.-R. Tang, Y.-J. Xu, *J. Mater. Chem. A* 6 (2018) 4590–4604.
  - [22] M.-Q. Yang, N. Zhang, Y. Wang, Y.-J. Xu, *J. Catal.* 346 (2017) 21–29.
  - [23] Q. Quan, X. Lin, N. Zhang, Y.-J. Xu, *Nanoscale* 9 (2017) 2398–2416.
  - [24] H.-P. Cong, J.-F. Chen, S.-H. Yu, *Chem. Soc. Rev.* 43 (2014) 7295–7325.
  - [25] B. Qiu, M. Xing, J. Zhang, *J. Am. Chem. Soc.* 136 (2014) 5852–5855.
  - [26] R. Wang, K.-Q. Lu, F. Zhang, Z.-R. Tang, Y.-J. Xu, *Appl. Catal. B* 233 (2018) 11–18.
  - [27] W. Han, L. Ren, L. Gong, X. Qi, Y. Liu, L. Yang, X. Wei, J. Zhong, *ACS Sustain. Chem. Eng.* 2 (2014) 741–748.
  - [28] K.-Q. Lu, L. Yuan, X. Xin, Y.-J. Xu, *Appl. Catal. B* 226 (2018) 16–22.
  - [29] M.-Q. Yang, X. Pan, N. Zhang, Y.-J. Xu, *CrystEngComm* 15 (2013) 6819–6828.
  - [30] K.-Q. Lu, N. Zhang, C. Han, F. Li, Z. Chen, Y.-J. Xu, *J. Phys. Chem. C* 120 (2016) 27091–27103.
  - [31] N. Zhang, M.-Q. Yang, Z.-R. Tang, Y.-J. Xu, *ACS Nano* 8 (2014) 623–633.
  - [32] W. Chen, L. Yan, *Nanoscale* 3 (2011) 3132–3137.
  - [33] Y. Fan, W. Ma, D. Han, S. Gan, X. Dong, L. Niu, *Adv. Mater.* 27 (2015) 3767–3773.
  - [34] N. Hao, X. Zhang, Z. Zhou, R. Hua, Y. Zhang, Q. Liu, J. Qian, H. Li, K. Wang, *Biosens. Bioelectron.* 97 (2017) 377–383.
  - [35] S. Ma, S. Zhan, Y. Jia, Q. Zhou, *ACS Appl. Mater. Interfaces* 7 (2015) 21875–21883.
  - [36] X. Cao, Z. Yin, H. Zhang, *Energy Environ. Sci.* 7 (2014) 1850–1865.
  - [37] X. Chen, G. Wu, J. Chen, X. Chen, Z. Xie, X. Wang, *J. Am. Chem. Soc.* 133 (2011) 3693–3695.
  - [38] B. Weng, Y.-J. Xu, *ACS Appl. Mater. Interfaces* 7 (2015) 27948–27958.
  - [39] X. Ning, W. Li, Y. Meng, D. Qin, J. Chen, X. Mao, Z. Xue, D. Shan, S. Devaramani, X. Liu, *Small* 14 (2018) 1703989.
  - [40] X. Xiao, L. Ge, C. Han, Y. Li, Z. Zhao, Y. Xin, S. Fang, L. Wu, P. Qiu, *Appl. Catal. B* 163 (2015) 564–572.
  - [41] N. Zhang, M. Li, C.F. Tan, C.K. Nuo Peh, T.C. Sum, G.W. Ho, J. Mater. Chem. A 5 (2017) 21570–21578.
  - [42] Y. Tang, Z. Jiang, J. Deng, D. Gong, Y. Lai, H.T. Tay, I.T.K. Joo, T.H. Lau, Z. Dong, Z. Chen, *ACS Appl. Mater. Interfaces* 4 (2012) 438–446.
  - [43] J. Cao, B. Luo, H. Lin, B. Xu, S. Chen, *J. Hazard. Mater.* 217–218 (2012) 107–115.
  - [44] H. Zhang, X. Fan, X. Quan, S. Chen, H. Yu, *Environ. Sci. Technol.* 45 (2011) 5731–5736.
  - [45] Q. Zhou, S. Ma, S. Zhan, *Appl. Catal. B* 224 (2018) 27–37.
  - [46] X. Zeng, D.T. McCarthy, A. Deletic, X. Zhang, *Adv. Funct. Mater.* 25 (2015) 4344–4351.
  - [47] Y. Jia, S. Zhan, S. Ma, Q. Zhou, *ACS Appl. Mater. Interfaces* 8 (2016) 6841–6851.
  - [48] N. Zhang, S. Xie, B. Weng, Y.-J. Xu, *J. Mater. Chem. A* 4 (2016) 18804–18814.
  - [49] C. Han, Z. Chen, N. Zhang, J.C. Colmenares, Y.-J. Xu, *Adv. Funct. Mater.* 25 (2015) 221–229.
  - [50] B. Weng, K.-Q. Lu, Z. Tang, H.M. Chen, Y.-J. Xu, *Nat. Commun.* 9 (2018) 1543.
  - [51] Q. Quan, S. Xie, B. Weng, Y. Wang, Y.-J. Xu, *Small* 14 (2018) 1704531.
  - [52] C. Han, Q. Quan, H.M. Chen, Y. Sun, Y.-J. Xu, *Small* 13 (2017) 1602947.
  - [53] C. An, J. Wang, W. Jiang, M. Zhang, X. Ming, S. Wang, Q. Zhang, *Nanoscale* 4 (2012) 5646–5650.
  - [54] C. Boerigter, U. Aslam, S. Linic, *ACS Nano* 10 (2016) 6108–6115.
  - [55] P. Christopher, H. Xin, S. Linic, *Nat. Chem.* 3 (2011) 467.
  - [56] W. Hou, S.B. Cronin, *Adv. Funct. Mater.* 23 (2013) 1612–1619.
  - [57] Z. Zhang, Y. Huang, K. Liu, L. Guo, Q. Yuan, B. Dong, *Adv. Mater.* 27 (2015) 5906–5914.
  - [58] Y. Zhang, C. Lin, Q. Lin, Y. Jin, Y. Wang, Z. Zhang, H. Lin, J. Long, X. Wang, *Appl. Catal. B* 235 (2018) 238–245.
  - [59] W. Wang, Y. Yu, T. An, G. Li, H.Y. Yip, J.C. Yu, P.K. Wong, *Environ. Sci. Technol.* 46 (2012) 4599–4606.